Microchimica Acta (2022) 189: 123
https://doi.org/10.1007/s00604-022-05232-6

ORIGINAL PAPER

Morphology and electrical properties of high-speed flexography-printed graphene

Rebecca R. Tafoya[1] · Michael A. Gallegos[1] · Julia R. Downing[2] · Livio Gamba[3] · Bryan Kaehr[1] · Eric N. Coker[1] · Mark C. Hersam[2] · Ethan B. Secor[3]

Received: 13 July 2021 / Accepted: 15 February 2022 / Published online: 28 February 2022

Abstract

Printed graphene electrodes have been demonstrated as a versatile platform for electrochemical sensing, with numerous examples of rapid sensor prototyping using laboratory-scale printing techniques such as inkjet and aerosol jet printing. To leverage these materials in a scalable production framework, higher-throughput printing methods are required with complementary advances in ink formulation. Flexography printing couples the attractive benefits of liquid-phase graphene printing with large-scale manufacturing. Here, we investigate graphene flexography for the fabrication of electrodes by analyzing the impacts of ink and process parameters on print quality and electrical properties. Characterization of the printed patterns reveals anisotropic structure due to striations along the print direction, which is related to viscous fingering of the ink. However, high-resolution imaging reveals a dense graphene network even in regions of sparse coverage, contributing to robust electrical properties even for the thinnest films (< 100 nm). Moreover, the mechanical and environmental sensitivity of the printed electrodes is characterized, with particular focus on atmospheric response and thermal hysteresis. Overall, this work reveals the conditions under which graphene inks can be employed for high-speed flexographic printing, which will facilitate the development of graphene-based sensors and related devices.

Keywords Flexible electronics · Printed electronics · Additive manufacturing · Flexographic printing · Graphene electrodes

Introduction

The integration of functional nanomaterials in scalable, liquid-phase printing processes offers opportunities for prototyping and production of low-cost, flexible, and disposable electronics and sensors [1]. Graphene is particularly versatile as a conductive, flexible, chemically inert material with high surface area that can be functionalized for targeted applications [2–4]. As a result, graphene inks have been employed for a variety of devices, including microscale heaters [5], supercapacitors [6], and environmental [7], chemical [8, 9], and biochemical sensors [10–14].

✉ Ethan B. Secor
esecor@iastate.edu

[1] Advanced Materials Laboratory, Sandia National Laboratories, Albuquerque, NM 87185, USA

[2] Department of Materials Science and Engineering, Northwestern University, Evanston, IL 60208, USA

[3] Department of Mechanical Engineering, Iowa State University, Ames, IA 50011, USA

Laboratory demonstrations of printed graphene devices are largely based on digital printing methods (e.g., inkjet and aerosol jet printing) due to their rapid prototyping compatibility and small-volume fabrication [9, 15–17]. However, as graphene-based technologies transition from laboratory demonstrations to production volumes, higher-throughput alternatives are imperative. The suitability of liquid-phase printing methods for both small-volume, lab-scale prototyping and high-throughput, roll-to-roll production is a key motivating factor for these technologies [6, 16, 18, 19]. In particular, roll-based contact printing methods using a physical master (e.g., flexography) offer a viable route to production-scale fabrication, with printing speeds on the order of tens of meters per minute [18, 20].

Flexographic printing is a high-throughput liquid-phase printing method suitable for roll-to-roll manufacturing [21]. During printing, ink fills an anilox roll containing engraved cells under the action of a doctor blade. This anilox roll is then brought into contact with the printing plate, which contains raised features defining the pattern. As the inked printing plate is brought into contact with the substrate, ink

is transferred to the substrate where it dries or otherwise solidifies to form the desired pattern. Flexographic printing features an elastomeric plate to define the pattern, enabling straightforward pattern redesign and tooling. This powerful advantage maintains the benefits of prototyping methods while providing the throughput speed of a roll-based printing press. Moreover, the flexible plate and occurrence of plate-substrate contact only in regions to be printed supports compatibility with a wide range of substrates and preprinted features. As a result, recent studies have focused on flexographic printing with nanomaterial inks for a variety of applications, including energy, sensing, electronics, security, and display technologies [18, 22–25]. The prevalent use of flexography for packaging materials (e.g., cardboard boxes, beverage cartons, and food packaging) positions it as a compelling platform for smart packaging with integrated sensing capabilities [26]. However, printing requirements for inks containing electronically functional material are distinct from those for pigmented inks used in conventional packaging. For example, microscopic nonuniformities in pattern reproduction are tolerable for graphics printing, but can lead to degraded or unexpected performance in electronic materials [24, 27]. Therefore, it is critical to evaluate the viability of flexography for functional 2D materials (e.g., graphene) and characterize how flexographic printing phenomena impact structure and properties.

A recent review paper by Tran et al. highlighted the challenge and noted the scarcity of laboratory demonstrations for high-speed printing of graphene [28]. Notably, a suitable graphene ink for volume-constrained methods such as gravure and flexographic printing requires excellent graphene dispersion quality, high concentration, and low viscosity. Achieving these three characteristics simultaneously requires consideration of the graphene flake size, which also affects functional properties such as conductivity. While previous efforts to print graphene by flexography deposited individual flakes to functionalize a surface, the requirement of continuous, conductive films requires much higher concentration ink and careful consideration of print morphology [29].

Here, we demonstrate flexographic printing of a graphene ink to achieve high-speed patterning of thin, conductive graphene patterns with ~ 100 µm patterning resolution. This work comprises three components. First, we discuss preparation and characterization of an ink suitable for flexographic printing, which demands high concentration while adhering to viscosity restrictions of the printing process. Second, a thorough characterization of the printing process for this ink reveals interactions between print speed, pattern geometry, and structural and functional properties of the resulting prints. Third, the stability of these printed graphene patterns is assessed, including sensitivity to bending, heat, and environmental conditions. Overall, we demonstrate printing of electrically continuous patterns at speeds of 30 m/min, achieving < 1 kΩ/sq sheet resistance for various pattern orientations and sizes.

Experimental

Ink preparation

Graphene was exfoliated from graphite by high shear mixing in ethanol with the stabilizing polymer ethyl cellulose (EC). A home-built, continuous flow shear mixing system (Silverson Machines, 200L inline mixer with a 1.5 HP motor) equipped with a square hole high shear screen was used to exfoliate flake graphite (Sigma-Aldrich, + 150 mesh) in a ~ 1% w/v ethanol-based solution of ethyl cellulose (EC, Sigma-Aldrich, 4 cP grade). Briefly, 200 g of EC were dissolved in 5 USG of ethanol (Decon Labs, 200-proof) at 50% mixer power, before 6 kg of graphite were added to the reactor. The power was then increased to 100% and continuous mixing proceeded for 96 h along a recirculating pathway. The resulting slurry was collected, and sedimentation of thick graphite flakes was carried out at ~ 10,000 rcf using an Avanti J26-XPI centrifuge (Beckman Coulter). The supernatant containing graphene nanosheets was decanted and subsequently combined with salt water (0.04 g/mL NaCl) in a ~ 2:1 v/v ratio to flocculate the graphene sheets, allowing them to be collected as a solid upon further centrifugation at ~ 12,000 rcf. Finally, the nanocomposite pellet comprised of enriched graphene/EC was washed with deionized water using vacuum filtration and dried to yield a fine powder containing ~ 40% wt. graphene as determined by thermogravimetric analysis. To prepare the flexographic graphene ink, 0.8 mL terpineol was first added to a glass vial, followed by 0.24 g of crushed graphene/EC powder, then 3.2 mL ethanol. The vial was sealed and bath sonicated at ~ 30 °C for 3 h total, with mixing by a vortex mixer for 1 min every ~ 30 min. This protocol results in a nominal composition of 6% w/v graphene/EC in 4:1 v/v ethanol/terpineol, with a graphene concentration of ~ 25 mg/mL.

Flexographic printing

Flexographic printing was performed with a Harper QD Printer roll-to-sheet flexography system. Springs rated at 51 lbs were used to maintain the contact force between the printing plate and substrate, and an anilox roll with 600 cpi was used. Polyimide sheets (Kapton FPC, 75 µm thick) were used for substrates, and printing was performed at ambient conditions (24 °C, 16% RH). For each printing run, ~ 0.5 mL ink was applied to the anilox roll and spread laterally to wet the entire width. The anilox roll and printing plate were thoroughly cleaned with isopropanol following each printing

run, and the anilox roll was further cleaned by bath sonication in water.

Characterization

Optical microscopy was performed with a Keyence VHX-7000 digital microscope. Optical profilometry measurements were performed with a Zygo 7100 optical profilometer. Electrical measurements were collected with a Keithley 2450 source measure unit. Basic electrical measurements (Fig. 6, Figure S5) were collected on simple line patterns using a 4-point probe configuration to eliminate contact resistance effects. For each resistance value, a bipolar I-V curve was collected and a linear fit was used to calculate the resistance. For metrics that account for sample geometry, the sample length and width were measured by optical microscopy and the cross-sectional area determined by optical profilometry. The measurement of cross-sectional area was performed prior to thermal curing, so a calibration sample of the same material on glass was used to account for thickness reduction during curing using contact profilometry, consistent with prior literature [19]. Single-device characteristics (Fig. 7, Figure S7) were collected using the 4-point probe method with a serpentine pattern containing 4 contact pads (inset, Fig. 7). Copper tape and silver paste were applied to the contact pads for secure connection of electrical leads during the extended tests. Humidity response data were collected with a Memmert HCP 108 Climate Chamber, and controlled O_2 studies used a ZR5 Zirox Oxygen Measuring System with gas composition controlled by two mass flow controllers. Viscosity data was collected using an Anton Paar MCR 302 Rheometer equipped with a cone and plate measurement system (25 mm, 2° cone). Electrochemical testing was performed with a PalmSens4 instrument on an interdigitated electrode pattern (E1) in a solution of 5 mM ferri/ferrocyanide with KCl as the electrolyte in varying concentrations. Cyclic voltammetry was done with 0.1 M KCl at scan speeds of 10, 20, 30, 40, and 50 mV/s. Electrochemical impedance spectroscopy was performed for KCl concentrations of 10^{-4}, 10^{-3}, 10^{-2}, and 0.1 M at 0 V DC bias. An AC bias of 0.05 V was applied at frequencies of 10^{-2}-10^{5} Hz. These parameters follow literature precedent [11] and are useful for probing electrical double layer effects that are nominally bias-independent, rather than redox kinetics that might occur at applied bias in more complex electrochemical systems such as batteries.

Error bars in general (Figs. 1, 2, 3, 4, 5 and 6) indicate the standard deviation of three measurements, although in some cases the error bars are masked by the data points because they are small. The data presented in Fig. 7 are single-device characterization tests and are not quantifying the device-to-device variability.

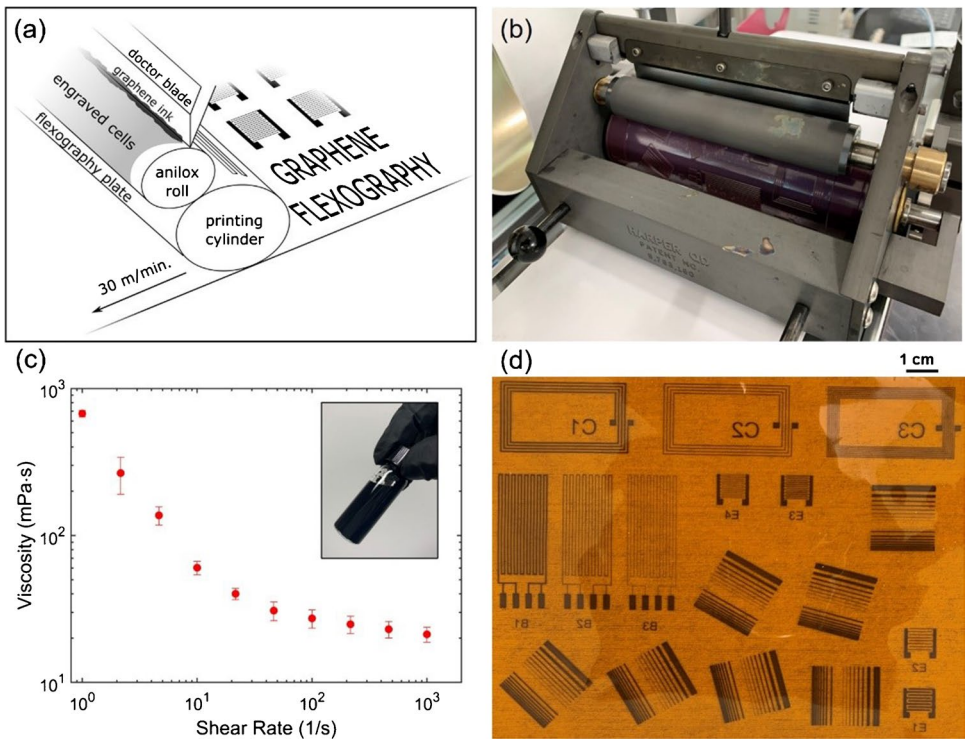

Fig. 1 Graphene flexography process schematic and overview. (**a**) Illustration of flexographic printing for functional graphene patterns, showing the printing cylinder, flexography plate, anilox roll, doctor blade, and ink. (**b**) Photograph of the flexography system. (**c**) Viscosity of the graphene flexography ink for shear rates of 1–1000 1/s; inset photograph of the graphene ink vial. (**d**) Photograph of the ~ 12 × 15 cm^2 graphene pattern printed by flexography on polyimide at a speed of 30 m/min

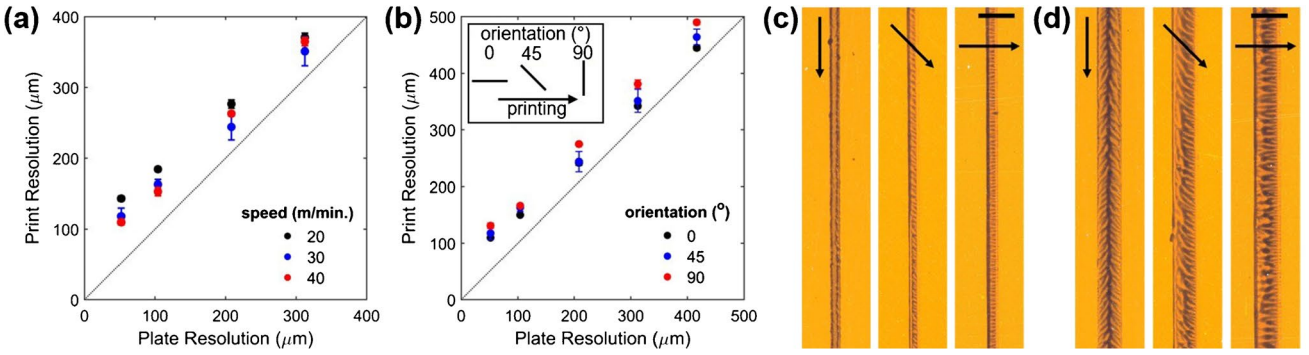

Fig. 2 Print characterization for graphene flexography. (**a**) Printed line resolution as a function of plate feature width for printing speeds of 20, 30, and 40 m/min (lines printed at 45° orientation angle with respect to the printing direction). (**b**) Printed line resolution plotted against plate feature width for printing at 30 m/min and orientations of 0, 45, and 90°. (**c**, **d**) Microscopy images showing printed lines corresponding to ~ 100 and ~ 300 μm plate features, respectively, at orientations of 0, 45, and 90° with respect to the printing direction (indicated by arrows). Scale bar: 500 microns

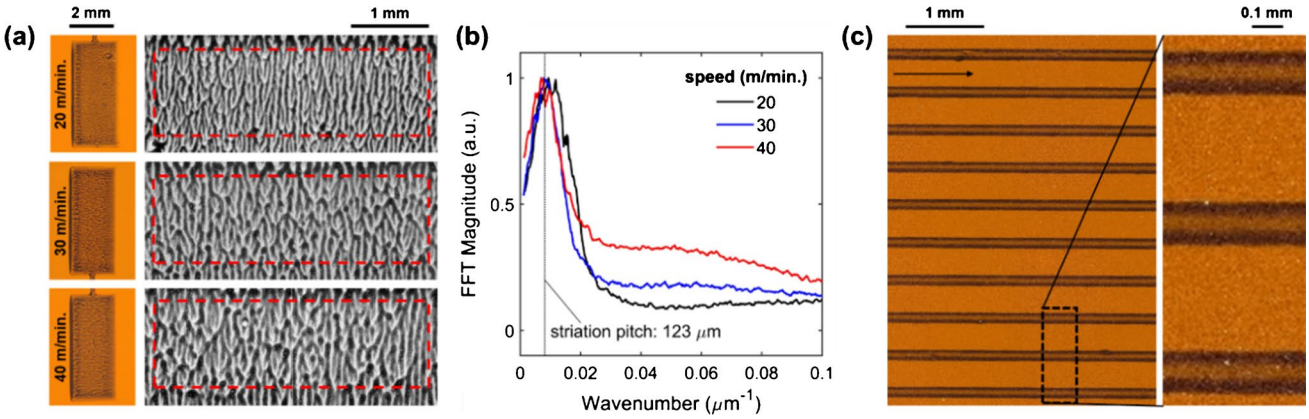

Fig. 3 Analysis of striation phenomena due to viscous fingering. (**a**) Microscopy images for pads printed at 20–40 m/min, including processed images used for FFT analysis showing the striation patterns. (**b**) One-dimensional FFT analysis for the images, showing a peak corresponding to the characteristic striation length scale at 100, 123, and 135 μm for printing at 20, 30, and 40 m/min, respectively. (**c**) Microscopy image showing consistent line morphology for ~ 150 μm lines oriented parallel to the printing direction

Results and discussion

Pattern design and system setup

The flexography printing system used for this study is described in Fig. 1a-b. The ink is applied to an anilox roll containing engraved cells to hold ink, and excess ink is removed from the surface using a doctor blade as the roll rotates. The anilox roll is then brought into contact with the flexographic plate, which is an elastomeric plate wrapped around the print cylinder containing relief (i.e., raised) features to define the printed pattern. Once the plate is brought into contact with the substrate, ink is transferred from the raised patterns onto the substrate in the defined geometry.

Graphene was prepared by high shear mixing from flake graphite in the presence of ethyl cellulose, yielding flakes with lateral dimensions of ~ 100–500 nm and thicknesses of ~ 1–5 nm (Figure S1, Figure S2). The ethyl cellulose acts as an exfoliation aid and dispersant, providing excellent colloidal stability and straightforward dispersion in simple and benign organic solvents (e.g., ethanol). The graphene ink used for this study contained 6% w/v graphene/EC dispersed in a solvent containing 4:1 v/v ethanol/terpineol. This formulation results in a black, shear-thinning graphene dispersion with a viscosity of 60 mPa·s at a shear rate of 10 1/s, which is suitable for flexography (Fig. 1c). Here, the terpineol serves as a low volatility cosolvent to mitigate rapid drying of the ink during handling. This material and solvent system is adapted from prior work [19, 30], and is known to exhibit robust, high electrical conductivity even for thin

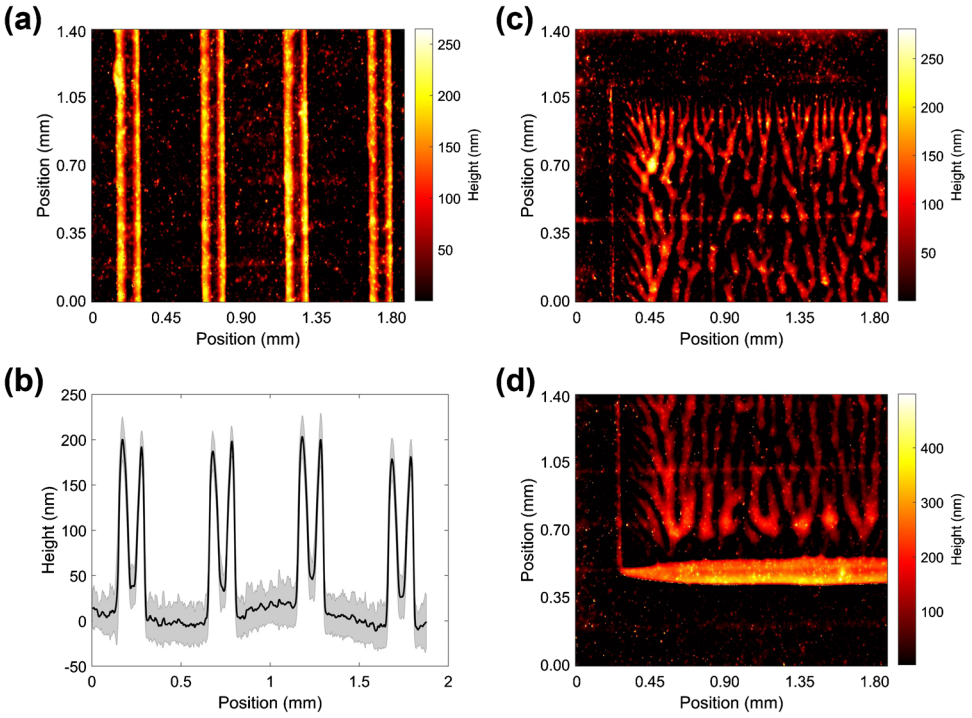

Fig. 4 Optical profilometry data showing the topography of graphene patterns prior to curing. (**a**, **b**) Height map and averaged profile, respectively, for narrow lines oriented along the printing direction. (**c**, **d**) Topography data for the leading and trailing edges, respectively, of a larger printed area showing material buildup

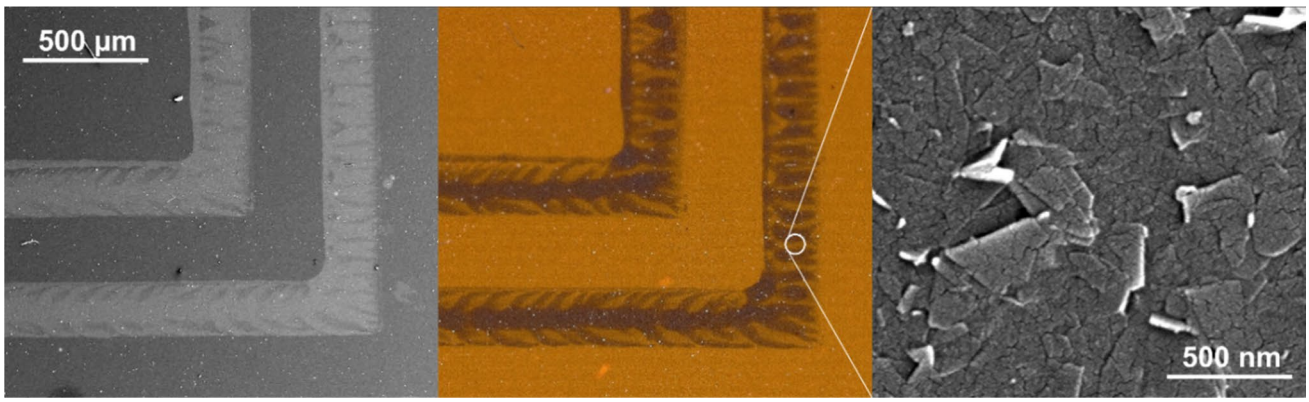

Fig. 5 Scanning electron microscopy analysis of pattern striations. Electron and optical micrographs of a printed corner feature showing the characteristic striations, along with high-resolution imaging in a sparse region that still reveals a dense network of graphene flakes

patterns below 100 nm in thickness. To evaluate printing performance, a test pattern was defined containing calibration line patterns and functional test structures, as shown in Fig. 1d, showcasing the high-speed, large-area printing capability of flexography.

Print morphology

During flexographic printing, the print speed is a key parameter that affects printing resolution and morphology [31]. For this study, graphene printing was performed at print speeds of 20, 30, and 40 m/min to evaluate the print resolution and morphology effects (Fig. 2a, Figure S3). During printing, the pattern transferred to the substrate is larger than the relief pattern on the printed plate. Thus, upon contact between the roll and substrate, ink is forced outward from the contact point and wets a wider area of the substrate [32]. Printing at 30 m/min resulted in ~ 50 µm excess pattern width, such that the smaller plate feature of 50 µm resulted in a printed feature width of ~ 100 µm. This phenomenon is consistent across different feature widths and print orientations (Fig. 2b, Figure S4). Here, the higher printing speeds of 30 m/min and 40 m/min resulted in consistently better line width definition compared to the slower (20 m/min) print speed, with the slower speed resulting in line broadening of ~ 75 µm.

Microscopy images in Fig. 2c-d show morphological features at a smaller length scale than the patterned lines. These

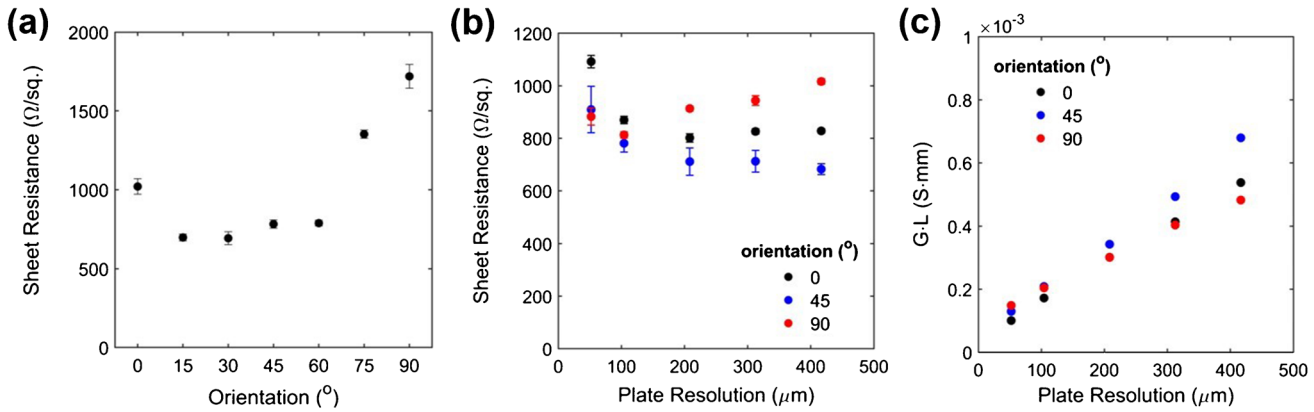

Fig. 6 Electrical characterization of flexographically printed graphene lines. (**a**) Sheet resistance of lines plotted against orientation, showing consistent electrical properties over a broad range from 15–60° line orientation. (**b**) Sheet resistance as a function of flexography plate resolution for narrow lines, showing some dependence on both the pattern width and line orientation. (**c**) Product of conductance and length plotted as a function of flexography plate resolution, showing an approximately linear dependence

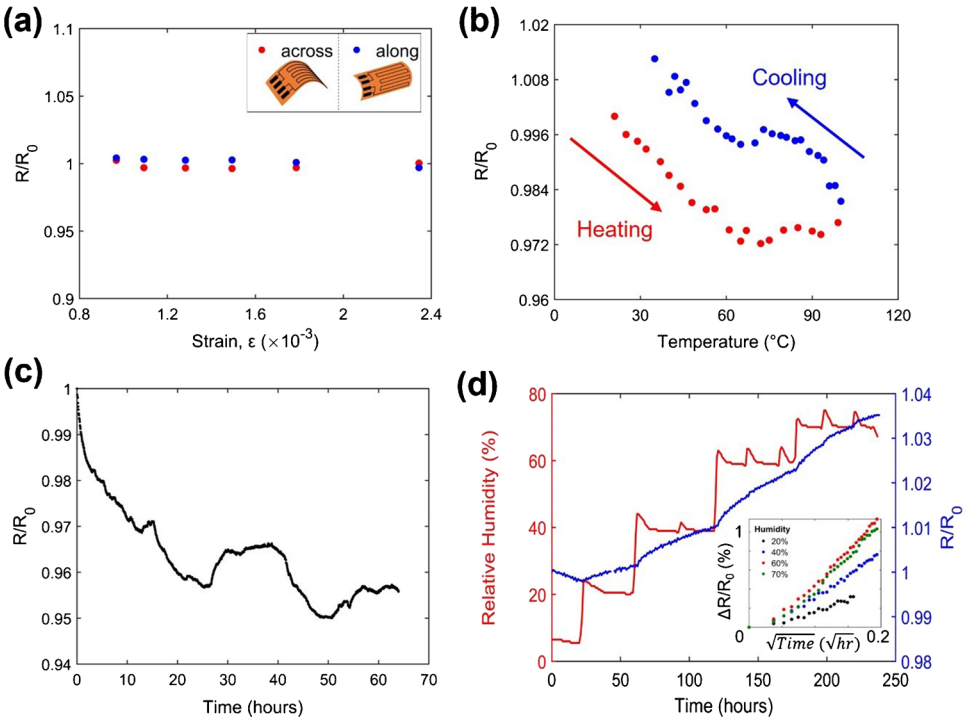

Fig. 7 Mechanical and environmental properties of graphene patterns from single-device measurements. (**a**) Normalized resistance plotted against bending strain for measurements taken in the bent state. (**b**) Effect of heating on the resistance of graphene patterns, showing a small reduction in resistance upon heating due to the negative temperature coefficient of resistivity, with hysteresis evident upon cooling. (**c**) Material equilibration in ambient following heating, showing a gradual reduction in resistance over 24–48 h. (**d**) Response of electrical properties to variations in humidity, showing an increase in resistance with increased humidity and a square root time response suggestive of Fickian diffusion (inset)

striations aligned with the printing direction are commonly observed in flexographic printing and result from an instability as air fingers penetrate the ink bridge as the printing plate and substrate separate [22]. This viscous fingering or ribbing effect causes anisotropy in the printed pattern, as the striations are oriented along the printing direction and furthermore result in asymmetric features on the leading and trailing edges of the ink deposit (Fig. 2d) [24].

Figure 3 shows the striations due to viscous fingering for equivalent film patterns printed at 20, 30 and 40 m/min (Figure S5). To characterize these patterns, a grayscale image of each pattern was analyzed (Fig. 3a) using a one-dimensional fast Fourier transform (FFT) aligned across the printing orientation. As shown in Fig. 3b, this provides a characteristic length scale for the striations, with values of 100, 123, and 135 μm for printing speeds of 20, 30, and 40 m/min., respectively. Here, as the printing speed is increased, the characteristic pitch of the striations also increases. This observation contrasts with previous results for Newtonian fluids, for which the viscous fingering length scales as the inverse square root of the capillary number resulting in a smaller striation pitch with increasing print velocity [22].

Interestingly, as the patterning length-scale approaches that of the striations, more consistent line morphology is

observed. This behavior is evident for the narrow lines patterned parallel to the print direction, as shown in detail in Fig. 3c (Figure S6). Here, the confinement of fluid into a ~ 150 μm wide trace couples with the characteristic striation length scale of similar magnitude to produce a consistent profile. The height profile is analyzed using optical profilometry, as shown in Fig. 4a-b. This measurement is performed prior to curing, and a separate test reveals a thickness reduction to 55% of the as-printed value following curing. Here, the line edges are ~ 200 nm thick, separated by a ~ 40 nm thick central region. This dimension is comparable to height variations in the more random striation patterns formed in the larger area figures (Fig. 4c-d), which are dominated by ink buildup on the trailing edge. Importantly, even in the thinner regions, sufficient material is deposited to form electrically continuous patterns. The improved control over striation morphology for confined features could potentially allow useful tailoring of the viscous fingering effect, analogous to exploitation of the coffee ring effect in inkjet printing to enhance performance in select applications [15].

The effect of striations on functional performance is an important research question impacting the application of flexography for printed electronics. If sparse regions lose continuity or exhibit significantly reduced conductivity due to percolation effects, electrical properties could be adversely affected. However, thinner regions could also be desirable for sensing applications due to the large, exposed surface area of the film. Moreover, the thin nature of the graphene flakes promotes efficient percolation compared to nanoparticles, and the ethyl cellulose dispersant has previously been shown to support continuous film formation below 50 nm [16, 19]. Indeed, scanning electron microscopy reveals that the graphene ink forms a dense, interconnected network of flakes even in these optically sparse regions (Fig. 5).

Electrical functionality

Here, the effect of striations on electrical properties is characterized. Despite the thin nature of the graphene film in some regions, electrical continuity of the patterns is maintained. Based on prior studies, the graphene/ethyl cellulose ink can exhibit thickness-dependent resistivity for films thinner than 50 nm [16]. For a more thorough understanding of coupling between the print morphology and electrical properties, the resistance of wide line patterns was measured for different orientations of the line with respect to the printing direction, as shown in Fig. 6a. Across a wide range of orientation angles from 15–60°, a consistently low sheet resistance of ~ 700 Ω/sq was observed. When the printing direction was aligned with the line (orientation angle of 0°), the resulting sheet resistance was nearly 50% higher, or ~ 1020 Ω/sq. For high orientation angles of 75 and 90°, the sheet resistance exhibits a more dramatic increase, with a maximum value of ~ 1720 Ω/sq, which is ~ 2.5-fold higher than that for the optimal orientation. Consequently, pattern orientation is an important design consideration for graphene flexographic printing. Nevertheless, the broad range of orientations supporting consistent electrical properties allows printing of right-angle patterns with uniform properties using either a 45° orientation or 30° and 60° orientations.

While the wide line patterns show clear variation in electrical properties based on print orientation, edge effects in the deposition can also play an important role for narrower lines. Ink buildup on the trailing edge of the print leads to pattern width dependence in the electrical properties for patterns transverse to the print direction. It is also important to consider line broadening effects in pattern design since higher resolution features exhibit proportionally larger spreading following printing. Figure 6b shows the manifestation of broadening effects for different print orientations. For the 45° orientation, the sheet resistance exhibits a decrease as the pattern feature width increases, because the deposited ink volume is more closely related to the pattern size than the final printed size. However, for the 90° orientation, the sheet resistance increases for larger pattern widths, which is attributed to ink buildup at the trailing edge of the printed line, as illustrated in Figs. 2c-d and 4d.

To normalize conductance for line broadening and understand the effects of ink buildup along the trailing edge, Fig. 6c shows the product of line conductance and length plotted as a function of defined width (the inverse of the more typical resistance per length value, shown in Figure S7). A linear slope for this plot indicates a direct correlation between the pattern width and the electrical conductance, such that higher conductance patterns can be straightforwardly designed by varying the geometry as is evident for features printed with the 45° orientation. The sharpest deviation from this behavior occurs for lines printed with the 90° orientation, for which the striations are aligned transverse to the conducting path. In this case, the plot exhibits a lower slope, suggesting incremental increases in pattern width are less effective at improving conductance. Moreover, the nonzero intercept correlates to the effect of ink buildup along the trailing edge, as this dense feature exhibits comparable width regardless of the pattern width.

While a direct measurement of line thickness was not possible for these thin patterns following curing due to the rough nature of the Kapton substrate, optical profilometry was performed prior to curing. Wide line patterns printed with 0, 45, and 90° orientation exhibited as-printed thicknesses of ~ 90 nm. Based on a measured reduction in thickness during annealing to 55% of the as-printed thickness, the resulting conductivity values for 0, 45, and 90° orientations are 19,800, 27,900, and 11,400 S/m, respectively, which is consistent with prior studies using graphene/ethyl

cellulose [16]. Taking the striations into account, regions of < 20 nm thickness exist following annealing. The retention of high electrical conductivity for such thin patterns, even over a relatively rough substrate, is a notable feature of the graphene ink and can be attributed to the continuous coverage of material even in optically sparse regions (Figure S8). This continuity has been observed in prior studies [19] and validates the use of this ink for flexographic printing in which pattern inhomogeneities could disrupt electrical continuity for other materials. Here, the nanoscale 2D nature of the graphene flakes allows efficient overlap for charge transport. Notably, thin, conductive patterns of graphene have been previously demonstrated as viable candidates for biochemical sensing [11, 33, 34]. The graphene patterns can be functionalized with recognition groups to provide specific sensing functionality. In this case, the thin nature of the electrodes can provide a high surface area with potential for increased sensitivity.

Electrical stability

Given the interest in using graphene for sensor electrodes [15, 35], it is important to better understand the native properties of the material when subjected to various stressors such as mechanical deformation, heat, humidity, and atmospheric conditions (Fig. 7). First, a serpentine pattern was bent around cylinders with varying radii of curvature. As shown in Fig. 7a, measurements in the bent state show no significant change in electrical properties, consistent with prior results using this material [16]. To test thermal sensitivity, samples were heated on a hotplate to 100 °C in air. As expected for graphitic materials with a negative temperature coefficient of resistivity, the resistance decreases slightly upon heating (Fig. 7b). Interestingly, some hysteretic behavior is observed that is noticeable above 60 °C, with a slightly higher measured resistance following the thermal cycle. This elevated resistance settles over a timescale of 24–48 h, with some fluctuations attributed to day–night cycles for laboratory temperature and humidity (Fig. 7c). To further explore this phenomenon, the same test was repeated under Ar atmosphere where the sample was heated to 100 °C, cooled quickly, and then monitored for ~ 40 h. In this case, the resistance rose ~ 15% as the sample cooled over the first 1.5 h, after which it remained relatively stable (Figure S9a). This observation suggests that the gradual equilibration in ambient atmosphere could be a result of gas or vapor adsorption, for which the initial heating to 100 °C alters the equilibrium. Because oxygen has been suggested as a likely dopant for carbon nanomaterials [36], this test was repeated in a dry, oxygen-controlled environment. Here, the sample resistance is stable for oxygen concentrations in the range of 0 to 20% (Figure S9b). Finally, the electrical properties were monitored following heating in a controlled humidity environment. As shown in Fig. 7d, the sample resistance varies ~ 3% for relative humidity (RH) values of 20–70%. As with equilibration in ambient following heating, the response time is on the order of hours, and an approximate square root time dependence is observed, consistent with Fickian diffusion (Figure S9c-d). Altogether, these results reveal a more complex response to environmental conditions than is commonly acknowledged for printed graphene, which merits consideration during device design and further study to support reliable application.

Discussion and Context

The combination of print speed, resolution, and electrical conductivity achieved by this method is competitive with recent literature reports [28]. A print speed of 30 m/min achieved by flexography is orders of magnitude faster than traditional laboratory-based methods, such as inkjet, aerosol jet, and electrohydrodynamic jet printing [21]. The print resolution of ~ 100 μm achieved here is within the range expected for flexography, and while somewhat lower than precision methods such as aerosol jet printing, suitable for large-area electrodes. The electrical properties, with a conductivity as high as 27,900 S/m and sheet resistance of ~ 1 kΩ/□, are highly competitive for carbon-based inks. This is in line with graphene/EC inks using other printing methods (inkjet, gravure) [16, 19] and substantially better than more conventional carbon-based inks including graphite and carbon black [37]. Moreover, the retention of high conductivity and electrical continuity for very thin (< 100 nm) patterns is significant, as it allows a reduction in materials use compared to thick-film methods such as screen printing. This is frequently not observed for nanomaterial inks [38] and reflects the excellent colloidal properties that support uniform film formation and efficient stacking even for very thin patterns. To assess potential suitability for electrochemical sensing, an interdigitated electrode pattern was characterized by cyclic voltammetry and electrochemical impedance spectroscopy (Figure S10), following standard literature precedent [39]. While there is a series resistance on the order of 3 kΩ, this is lower than that of other printed graphene electrodes [11], and the device demonstrates sensitivity to the electrolyte concentration evidenced by an ~ 8 × change in total impedance as the electrolyte concentration is increased from 10^{-4} to 0.1 M [39]. Future functionalization with appropriate selective agents could thus position these electrodes for applications in biosensors [11].

Conclusion

Overall, we have demonstrated a promising platform for high-throughput fabrication of graphene electrodes based on flexographic printing. By using an ink based on small,

well-dispersed graphene flakes with an ethyl cellulose polymeric binder, patterns with ~ 100 µm resolution, < 1 kΩ/sq sheet resistance, and 27,900 ± 1,500 S/m electrical conductivity were printed with a speed of 30 m/min. This extends a graphene ink system that can be tailored for different printing methods, allowing more streamlined prototyping to production workflow. Importantly, the graphene composition offers broader potential for other circuit elements such as wireless antennas, flexible interconnects, and resistors. The 2D nature of graphene, coupled with the robust ink properties, resulted in reliable electrical conductivity in the printed patterns despite morphological heterogeneities common to the printing process (i.e., striations). Moreover, the thin, conductive patterns are suitable for high-throughput processing of low-cost, flexible, and disposable sensors. Further analysis of the humidity response of the deposited films could enable new insights toward the environmental stability of this material system for sensing applications.

Supplementary Information The online version contains supplementary material available at https://doi.org/10.1007/s00604-022-05232-6.

Acknowledgements This work was supported by the Harry S. Truman Fellowship through the Laboratory Directed Research and Development program at Sandia National Laboratories. This work was performed, in part, at the Center for Integrated Nanotechnologies, an Office of Science User Facility operated for the U.S. Department of Energy (DOE) Office of Science. Sandia National Laboratories is a multi-program laboratory managed and operated by National Technology and Engineering Solutions of Sandia, LLC, a wholly owned subsidiary of Honeywell International, Inc., for the US Department of Energy's National Nuclear Security Administration under contract DE-NA-0003525. This paper describes objective technical results and analysis. Any subjective views or opinions that might be expressed in the paper do not necessarily represent the views of the US Department of Energy or the United States Government. The authors would like to acknowledge support from Iowa State University, the National Science Foundation Scalable Nanomanufacturing Program (NSF CMMI-1727846 and NSF CMMI-2039268), and the National Science Foundation Future Manufacturing Program (NSF CMMI-2037026). Rheometry and thermogravimetric analysis were performed in the Materials Characterization and Imaging (MatCI) Facility at Northwestern University, which receives support from the National Science Foundation Materials Research Science and Engineering Center Program (NSF DMR-1720139).

Author contributions Ethan B. Secor contributed to conceptualization; Ethan B. Secor, Julia R. Downing, Rebecca R. Tafoya, Michael Gallegos, Eric N. Coker, and Livio Gamba provided methodology; Julia R. Downing, Rebecca R. Tafoya, Livio Gamba, and Ethan B. Secor performed formal analysis and investigation; Rebecca R. Tafoya and Ethan B. Secor performed writing—original draft preparation; Mark C. Hersam, Michael Gallegos, Bryan Kaehr, Julia R. Downing, and Eric N. Coker performed writing—review and editing; Mark C. Hersam, Ethan B. Secor, and Bryan Kaehr contributed to funding acquisition; Mark C. Hersam and Bryan Kaehr provided resources; Mark C. Hersam and Ethan B. Secor done supervision.

Funding Sandia National Laboratories, Laboratory Directed Research and Development Program; DOE Center for Integrated Nanotechnologies; National Science Foundation Scalable Nanomanufacturing Program; National Science Foundation Future Manufacturing Program.

Availability of data and material The datasets generated during and/or analyzed during the current study are available from the corresponding author on reasonable request.

Declarations

Conflicts of interest The authors declare no competing interest.

References

1. Sui X, Downing JR, Hersam MC, Chen J (2021) Additive manufacturing and applications of nanomaterial-based sensors. Mater Today 48:135–154. https://doi.org/10.1016/j.mattod.2021.02.001
2. Geim AK, Novoselov KS (2007) The rise of graphene. Nat Mater 6:183–191
3. Kim H, Ahn JH (2017) Graphene for flexible and wearable device applications. Carbon N Y 120:244–257. https://doi.org/10.1016/j.carbon.2017.05.041
4. Wisitsoraat A, Mensing JP, Karuwan C et al (2017) Printed organo-functionalized graphene for biosensing applications. Biosens Bioelectron 87:7–17. https://doi.org/10.1016/j.bios.2016.07.116
5. Xu L, Wang H, Wu Y et al (2021) A one-step approach to green and scalable production of graphene inks for printed flexible film heaters. Mater Chem Front 5:1895–1905. https://doi.org/10.1039/d0qm00803f
6. Chang Q, Li L, Sai L et al (2018) Water-soluble hybrid graphene ink for gravure-printed planar supercapacitors. Adv Electron Mater 4:1–10. https://doi.org/10.1002/aelm.201800059
7. Meng FL, Guo Z, Huang XJ (2015) Graphene-based hybrids for chemiresistive gas sensors. Trends Anal Chem 68:37–47. https://doi.org/10.1016/j.trac.2015.02.008
8. Zhang Q, An C, Fan S et al (2018) Flexible gas sensor based on graphene/ethyl cellulose nanocomposite with ultra-low strain response for volatile organic compounds rapid detection. Nanotechnology 29:285501. https://doi.org/10.1088/1361-6528/aabf2f
9. Le T, Lakafosis V, Lin Z, et al (2012) Inkjet-printed graphene-based wireless gas sensor modules. IEEE 62nd Electron Components Technol Conf 1003–1008. https://doi.org/10.1109/ECTC.2012.6248958
10. Sethi J, Van Bulck M, Suhail A et al (2020) A label-free biosensor based on graphene and reduced graphene oxide dual-layer for electrochemical determination of beta-amyloid biomarkers. Microchim Acta 187:288. https://doi.org/10.1007/s00604-020-04267-x
11. Parate K, Rangnekar SV, Jing D et al (2020) Aerosol-jet-printed graphene immunosensor for label-free cytokine monitoring in serum. ACS Appl Mater Interfaces 12:8592–8603. https://doi.org/10.1021/acsami.9b22183
12. Sanati A, Jalali M, Raeissi K et al (2019) A review on recent advancements in electrochemical biosensing using carbonaceous nanomaterials. Microchim Acta 186:773. https://doi.org/10.1007/s00604-019-3854-2
13. Gomez FJV, Martín A, Silva MF, Escarpa A (2015) Screen-printed electrodes modified with carbon nanotubes or graphene for simultaneous determination of melatonin and serotonin. Microchim Acta 182:1925–1931. https://doi.org/10.1007/s00604-015-1520-x
14. Xu J, Wang Y, Hu S (2017) Nanocomposites of graphene and graphene oxides: Synthesis, molecular functionalization and application in electrochemical sensors and biosensors.

A reiew. Microchim Acta 184:1–44. https://doi.org/10.1007/s00604-016-2007-0
15 Parate K, Pola CC, Rangnekar SV et al (2020) Aerosol-jet-printed graphene electrochemical histamine sensors for food safety monitoring. 2D Mater 7:034002. https://doi.org/10.1088/2053-1583/ab8919
16. Secor EB, Prabhumirashi PL, Puntambekar K et al (2013) Inkjet printing of high conductivity, flexible graphene patterns. J Phys Chem Lett 4:1347–1351. https://doi.org/10.1021/jz400644c
17. Dongmo LM, Guenang LS, Jiokeng SLZ et al (2021) A new sensor based on an amino-montmorillonite-modified inkjet-printed graphene electrode for the voltammetric determination of gentisic acid. Microchim Acta 188:36. https://doi.org/10.1007/s00604-020-04651-7
18. Khan S, Lorenzelli L, Dahiya RS (2015) Technologies for printing sensors and electronics over large flexible substrates: A review. IEEE Sens J 15:3164–3185. https://doi.org/10.1109/JSEN.2014.2375203
19. Secor EB, Lim S, Zhang H et al (2014) Gravure printing of graphene for large-area flexible electronics. Adv Mater 26:4533–4538. https://doi.org/10.1002/adma.201401052
20. Bonaccorso F, Bartolotta A, Coleman JN, Backes C (2016) 2D-crystal-based functional inks. Adv Mater 28:6136–6166. https://doi.org/10.1002/adma.201506410
21. Maddipatla D, Narakathu BB, Atashbar M (2020) Recent progress in manufacturing techniques of printed and flexible sensors: a review. Biosensors 10:199. https://doi.org/10.3390/bios10120199
22. Brumm P, Sauer H, Dörsam E (2019) Scaling behavior of pattern formation in the flexographic ink splitting process. Colloids and Interfaces 3:37. https://doi.org/10.3390/colloids3010037
23. Benson J, Fung CM, Lloyd JS et al (2015) Direct patterning of gold nanoparticles using flexographic printing for biosensing applications. Nanoscale Res Lett 10:1–8. https://doi.org/10.1186/s11671-015-0835-1
24. Morgan ML, Holder A, Curtis DJ, Deganello D (2018) Formulation, characterisation and flexographic printing of novel Boger fluids to assess the effects of ink elasticity on print uniformity. Rheol Acta 57:105–112. https://doi.org/10.1007/s00397-017-1061-9
25. Kempa H, Hambsch M, Reuter K et al (2011) Complementary ring oscillator exclusively prepared by means of gravure and flexographic printing. IEEE Trans Electron Devices 58:2765–2769. https://doi.org/10.1109/TED.2011.2153856
26. Chen S, Brahma S, Mackay J et al (2020) The role of smart packaging system in food supply chain. J Food Sci 85:517–525. https://doi.org/10.1111/1750-3841.15046
27. Morgan ML, Curtis DJ, Deganello D (2019) Control of morphological and electrical properties of flexographic printed electronics through tailored ink rheology. Org Electron 73:212–218. https://doi.org/10.1016/j.orgel.2019.05.027
28. Tran TS, Dutta NK, Choudhury NR (2018) Graphene inks for printed flexible electronics: graphene dispersions, ink formulations, printing techniques and applications. Adv Colloid Interface Sci 261:41–61. https://doi.org/10.1016/j.cis.2018.09.003
29. Watson TM, Deganello D, Gethin DT (2014) Flexographic printing of graphene nanoplatelet ink to replace platinum as counter electrode catalyst in flexible dye sensitised solar cell. Energy Mater Mater Sci Eng Energy Syst 9:86–90. https://doi.org/10.1179/1433075X14Y.0000000203
30. Liang YT, Hersam MC (2010) Highly concentrated graphene solutions via polymer enhanced solvent exfoliation and iterative solvent exchange. J Am Chem Soc 132:17661–17663. https://doi.org/10.1021/ja107661g
31. Kumar S (2015) Liquid transfer in printing processes: liquid bridges with moving contact lines. Annu Rev Fluid Mech 47:67–94. https://doi.org/10.1146/annurev-fluid-010814-014620
32. Joyce M, Avuthu SGR, Emamian S et al (2014) Contribution of flexo process variables to fine line Ag electrode performance. Int J Eng Res Te 3:1645–1656
33. Yamuna A, Sundaresan P, Chen SM (2019) Ethylcellulose assisted exfoliation of graphite by the ultrasound emulsification: an application in electrochemical acebutolol sensor. Ultrason Sonochem 59:104720. https://doi.org/10.1016/j.ultsonch.2019.104720
34. Kim DS, Jeong JM, Park HJ et al (2021) Highly concentrated, conductive, defect-free graphene ink for screen-printed sensor application. Nano-Micro Lett 13:87. https://doi.org/10.1007/s40820-021-00617-3
35. Kirchner EM, Hirsch T (2020) Recent developments in carbon-based two-dimensional materials: synthesis and modification aspects for electrochemical sensors. Microchim Acta 187:441. https://doi.org/10.1007/s00604-020-04415-3
36. Ryu S, Liu L, Berciaud S et al (2010) Atmospheric oxygen binding and hole doping in deformed graphene on a SiO2 substrate. Nano Lett 10:4944–4951. https://doi.org/10.1021/nl1029607
37. Phillips C, Al-Ahmadi A, Potts SJ et al (2017) The effect of graphite and carbon black ratios on conductive ink performance. J Mater Sci 52:9520–9530. https://doi.org/10.1007/s10853-017-1114-6
38. Karagiannidis PG, Hodge SA, Lombardi L et al (2017) Microfluidization of graphite and formulation of graphene-based conductive inks. ACS Nano 11:2742–2755. https://doi.org/10.1021/acsnano.6b07735
39. Hondred JA, Stromberg LR, Mosher CL et al (2017) High-resolution graphene films for electrochemical sensing via inkjet maskless lithography. ACS Nano 11:9836–9845. https://doi.org/10.1021/acsnano.7b03554